Journal of Materials Chemistry B

ROYAL SOCIETY OF CHEMISTRY

PAPER

View Article Online
View Journal | View Issue

Cite this: J. Mater. Chem. B, 2025, 13, 13048

Gadolinium-doped carbon dots derived from peanut shell waste for bioimaging applications

Federica Mancini,[a] Arianna Menichetti,[b] Alessio Adamiano,[a] Marco Montalti,[b] Konstantin Paliienko,[cd] Alain Géloën,[e] Vladimir Lysenko[f] and Michele Iafisco *[a]

Received 13th June 2025,
Accepted 1st September 2025

DOI: 10.1039/d5tb01420d

rsc.li/materials-b

This study explores the synthesis, characterization, and biomedical potential of carbon dots (CDs) derived from food industry by-products. Gd-doped CDs were synthesized using peanut shells as a sustainable carbon source. The resulting CDs were smaller than 20 nm in size and exhibited a negative zeta potential. FTIR analysis revealed the presence of polar surface functional groups, which contributed to excellent dispersibility in water and other polar solvents. Photophysical characterization showed strong absorption in the UV region and blue fluorescence under UV irradiation. Gd^{3+} doping enhanced the absorption intensity in the 2–5.5 eV range and partially quenched fluorescence at high concentrations. The MRI performance of Gd-doped CDs as a positive contrast agent was assessed using 7 and 11.7 Tesla scanners. Despite their lower Gd content, Gd-doped CDs exhibited signal intensities comparable to other Gd-based contrast agents. Furthermore, cytotoxicity assays confirmed their biocompatibility with A549 cells at concentrations of up to 0.1 mg mL^{-1}. This approach not only provides an innovative and environmentally sustainable strategy for valorising food industry waste within a circular economy framework, but also introduces a new biocompatible material for MRI imaging applications.

1. Introduction

Considering growing environmental challenges and increasing resource scarcity, the concept of the circular economy has emerged as a promising alternative to the traditional linear model of production and consumption.[1] Unlike the linear economy, which follows a 'take-make-dispose' approach, the circular economy aims to minimize waste and maximize resource efficiency by promoting reuse, recycling, and regeneration.[2,3] This model represents a paradigm shift towards sustainability, emphasising the preservation of natural resources, the reduction of environmental impact, and the creation of new economic opportunities.

One promising strategy in the pursuit of sustainable materials is the valorisation of by-products from the food industry.[4] In this context, carbon dots (CDs) synthesised from food by-products have gained significant attention. CDs are nanoscale carbon-based particles that exhibit exceptional optical, electronic, and magnetic properties, making them attractive for various biomedical and technological applications.[5–7] In recent years, CDs have been studied for bioimaging and diagnostic applications, due to their intrinsic luminescence, low toxicity, and ease of synthesis.[8–11] These nanomaterials can be prepared from different types of food-derived waste materials through methods such as hydrothermal, microwave-assisted, or solvothermal synthesis, which facilitate the conversion of organic precursors into fluorescent nanomaterials.[12,13] Several different food by-products have been explored for CD preparation including orange and watermelon waste peels,[14,15] onion waste[16] and fennel seeds.[17]

Magnetic resonance imaging (MRI) is a non-invasive and versatile imaging modality that provides detailed anatomical and functional information.[18] In this context, gadolinium (Gd), a lanthanide element, is widely used in MRI contrast agents and for enhancing radiosensitization due to its unique physical and chemical properties.[19–21] The Gd(3+) ion is particularly suited for MRI applications because of its long electron spin relaxation time (10^{-9} s) and high magnetic moment,[22] both of which contribute to superior contrast in MRI scans. Gd chelates,

[a] Institute of Science, Technology and Sustainability for Ceramics (ISSMC), National Research Council (CNR), 48018, Faenza, RA, Italy. E-mail: michele.iafisco@issmc.cnr.it
[b] Department of Chemistry "Giacomo Ciamician", Alma Mater Studiorum-Università di Bologna, 40126, Bologna, Italy
[c] Corporation Science Park, Taras Shevchenko University of Kyiv, Kyiv, 01033, Ukraine
[d] Palladin Institute of Biochemistry of the National Academy of Sciences of Ukraine, 9, Leontovicha Str, Kyiv, 01054, Ukraine
[e] Claude Bernard University of Lyon, UMR Ecologie Microbienne Lyon (LEM), CNRS 5557, INRAE 1418, VetAgro Sup, 69622, Villeurbanne, France
[f] Claude Bernard University of Lyon, Light Matter Institute (ILM), CNRS UMR 5306, 69622, Villeurbanne, France

such as gadopentetate dimeglumine (Gd-DTPA) and gadoterate meglumine (Gd-DOTA), are commonly employed due to their high relaxivity.[23] These agents work by shortening the longitudinal relaxation time (T_1) of nearby water protons, resulting in enhanced signal intensity in T_1-weighted images and improved tissue contrast. However, free Gd ions can be highly toxic to living organisms.[24,25] As a result, Gd-doped CDs (Gd-CDs) represent a valuable and safer alternative to these compounds.[26–28] Gd-CDs offer improved stability and a reduced risk of free Gd ion release compared to traditional chelates, potentially mitigating associated toxicities.[29–31]

Several types of Gd-CDs have been developed in recent years.[32–34] Gd-CDs were typically synthesized from chemical precursors using a one-step hydrothermal or solvothermal method with citric acid as the carbon source and a Gd-compound, such as gadolinium chloride or Gd-DTPA.[27,35–38] This approach generally ensures the efficient incorporation of Gd into carbon structures. However, it does not enable the valorization of existing biomasses and biowastes. To the best of our knowledge, very few examples of Gd-CDs produced from natural sources have been reported in the literature.[22,28,39]

This study investigates the synthesis, characterisation and application of Gd-CDs derived from food industry by-products as potential MRI contrast agents. Specifically, we describe the synthesis of Gd-free (PSC) and Gd-doped (PSGd) CDs from peanut shells. In comparison to previous studies on Gd-CDs from food industry by-products, this study explores the use of fruit peels, which, compared to other waste materials,[40] account for approximately 1750 million tons of discarded fruit and vegetable by-products worldwide each year.[41] Thanks to the MRI contrast-enhancing capabilities of Gd, these materials demonstrated improved imaging performance with significant potential for advancing biomedical diagnostics. Furthermore, this approach offers an innovative and environmentally sustainable strategy by converting discarded food industry by-products, such as peanut shells, into high-value nanomaterials, aligning with circular economy principles.

2. Methodology

2.1 Materials

Peanuts were purchased from a local market, and the shells were separated manually. Ultrapure water was produced with an Arium© Pro instrument from Sartorius (Goettingen, Germany). Ammonia aqueous solution (NH_4OH, ACS reagent, 28–30% solution) was purchased from Merck (Darmstadt, Germany). Gadolinium chloride hexahydrate ($GdCl_3{\cdot}6H_2O$, 99%) was purchased from Sigma Aldrich (St. Louis, MO, USA). 9,10-Diphenylanthracene (>99%) was purchased from Sigma Aldrich (St. Louis, MO, USA). A dialysis membrane with a molecular weight cut off of 3500 Da (Spectra/Por® dialysis membrane, standard RC tubing, flat width 18 mm, volume per length 1.1 mL cm^{-1}) was purchased from Repligen (Waltham, Massachusetts, USA).

2.2 Synthesis of CDs

Gd-doped (PSGd) and Gd-free (PSC) CDs were prepared through a multi-step process according to the scheme reported in Fig. 1. In Step 1, peanut shells were ground at 5000 rpm for 10 minutes using a blade mill (IKA MultiDrive basic, IKA®-Werke GmbH, Staufen, Germany) equipped with blades for fibrous materials (IKA MultiDrive accessories: MultiDrive MI 250 Milling chamber and MultiDrive MI 250.2 star-shaped cutter). In Step 2, for PSGd synthesis, 150 mL of 0.1 or 0.5 M $GdCl_3$ solution were added to 50 g of the peanut shell powder in a 500 mL round-bottom flask. The mixture was then refluxed at 100 °C for 1 hour to promote interaction between the source material and

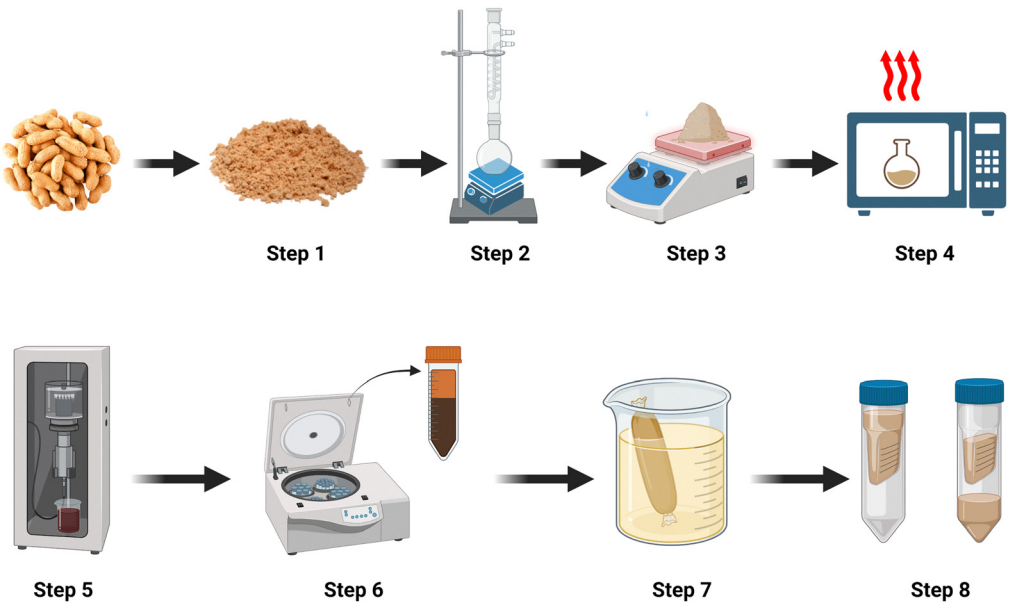

Fig. 1 Schematic illustration of the preparation process of Gd-doped and Gd-free CDs.

Gd^{3+} ions. The resulting materials were named PSGd 0.1 M and PSGd 0.5 M. For PSC synthesis, this step was carried out identically using 150 mL of water instead of the $GdCl_3$ solution. In Step 3, the product was dried in air at 100 °C for 3 hours. In Step 4, the dried product was mixed with 20 mL of 10 wt% NH_4OH solution in a 250 mL glass flask, and the mixture was heated in a domestic microwave oven (700 W consumption power) for 20 minutes. In Step 5, the microwaved product was suspended in 200 mL of water and sonicated for 45 minutes at full power using a tip sonicator (Bandelin electronic, GM 2070 model, 70-Watt, 20 kHz). In Step 6, the ultrasonicated suspension was centrifuged at 3000 rcf for 3 hours in 50 mL tubes to remove the insoluble debris. The supernatant was then subjected to ultra-filtration using Vivaspin 20® spin concentrators (50 000 MWCO, PES membrane) and centrifuged at 2000 rcf for 30 minutes. In Step 7, the filtrate obtained from Step 6 was placed in dialysis membranes with a molecular weight cut-off of 3500 Da. Dialyzing membranes containing PSGd and PSC suspensions were placed separately in 10 L water tanks, with water being refreshed every 12 hours for 72 hours in the case of PSC or 120 hours for PSGd 0.1 and 0.5 M. In Step 8, PSC and PSGd samples were preconcentrated by centrifugation of the dialyzed dispersions using 3000 MWCO Vivaspin 20® PES membranes at 3000 rcf for 2 hours. For each sample, the filtrate and retentate were collected for further analysis.

2.3 CD characterization

Proton magnetic resonance relaxation time T_1 of the CDs in water suspensions was measured using a Bruker Minispec MQ60 nuclear magnetic resonance analyser (Bruker, Billerica, MA, USA), operating at 40 °C under a magnetic field of 1.4 T (60 MHz). Aliquots of 300 µl were taken from concentrated samples and measured in NMR glass tubes. The Gd content of the suspensions was determined by ICP-MS analysis using a PerkinElmer NexION2000 (PerkinElmer, Waltham, MA, USA) equipped with an Elemental Scientific Inc. SC-FAST sample introduction system. Measurements were done in a standard mode with argon plasma. The calibration curve was done using the PlasmaCAL® Gadolinium standard for ICP-AES and -MS analysis. The samples were prepared by dilution in an aqueous solution of 1% v/v HNO_3 with 5 ppb of indium as an internal standard. The experimental data were expressed as the mean value ± standard deviation (SD) of several abundant Gd isotopes (^{156}Gd, ^{158}Gd, and ^{160}Gd) of n (n = 3) independent experiments. CD aqueous dispersions were analyzed through dynamic light scattering (DLS) to determine the hydrodynamic diameter distribution and electrophoretic mobility (ζ-potential). DLS and ζ-potential analyses were performed after dilution using a Zetasizer Nano ZSP instrument (Malvern Instruments Ltd, Malvern, UK). The hydrodynamic diameter distribution of the samples was measured using a carbon dot refractive index (1.55) and water refractive index (1.33) as working parameters for the samples and the solvent, respectively. Size results are reported as the *Z*-average of the hydrodynamic diameter of the particles of three measurements at 25 °C with at least 10 runs. ζ-Potentials were quantified as the electrophoretic mobility of three separate measurements (maximum 100 runs each) at 25 °C by laser Doppler velocimetry using a disposable electrophoretic cell (DTS1061, Malvern Ltd, Worcestershire, UK) with the same sample and solvent parameters.

The concentration of CDs was estimated by freeze drying the samples and weighing the solid residue. The dry mass contents were found to be 7.8, 6.4 and 2.1 mg mL^{-1} for PSC, PSGd 0.1 M and PSGd 0.5 M, respectively. Freeze-dried CDs were further characterized using powder X-ray diffraction (PXRD) and Fourier transform infrared (FT-IR) spectroscopy. The PXRD pattern was collected with a D8 Advance diffractometer (Bruker, Karlsruhe, Germany). Cu Kα X-rays were generated at 40 kV and 40 mA. The pattern was collected in the 10–60° 2θ range with a step size of 0.02° 2θ and a counting time of 0.5 s. FT-IR spectra were recorded in the attenuated total reflectance (ATR) mode with a Nicolet iS5 spectrometer (Thermo Fisher Scientific Inc., Waltham, MA, USA) using an iD7 diamond ATR accessory. The spectra were recorded with a resolution of 4 cm^{-1} by accumulation of 32 scans covering the 4000 to 400 cm^{-1} spectral range.

Photophysical characterization of CDs was performed on as-synthesized suspensions after dilution. CD absorption spectra were recorded using a PerkinElmer Lambda 650 UV/vis spectrometer (PerkinElmer, Shelton, CT, USA). In addition, spectral deconvolution was performed, after subtraction of an exponential-like baseline, in the full wavenumber range using ORIGIN 2018 software. The obtained UV-vis spectra were deconvolved into elementary Gaussian-like peaks. Emission spectra and 3D excitation and emission maps were recorded using a Horiba Fluoromax-4 spectrofluorometer (Horiba, Edison, NJ, USA). Emission lifetimes were obtained through time-correlated single photon counting (Edinburgh Instruments, Levington, UK). Emission lifetimes were obtained through time-correlated single photon counting (Edinburgh Instruments, Levington, UK). Fluorescence quantum yields were calculated using 9,10-diphenylanthracene as the standard, by means of the following equation:[42]

$$\Phi = \Phi_s \frac{I}{I_s} \frac{A_s}{A} \frac{n^2}{n_s^2} \quad (1)$$

where Φ is the quantum yield, Φ_s is the quantum yield of the standard, I is the integrated area of the emission spectrum of the sample and I_s is that of the standard, A is the absorbance at the excitation wavelength of the sample and A_s is that of the standard, and n is the refractive index of the solvent of the sample and n_s is that of the standard.

2.4 Cytotoxicity

Cell number measurements were performed using a non-destructive impedance-based technique called xCELLigence (ACEA Biosciences Inc., Biotek, Colmar, France). Cells were cultured on a special plate with electrodes at the bottom. The system measures the electrical impedance across interdigitated microelectrodes located at the bottom of the culture wells. Measurements were made by applying an alternative excitation signal (with a control voltage amplitude of 20 mV) at 3 different

frequencies (10, 25 and 50 kHz) through the microelectrodes in the E-plates while monitoring the voltage drop across the electrodes. The impedance data were processed over time, resulting in a cell index value. The cell index was related to factors such as cell number, cell surface area and adhesion strength. Of these factors, cell number was found to be the primary determinant of the cell index value for a given cell line, although changes in adhesion strength can also affect the cell index. The impedance measurement method used was non-destructive and allowed continuous real-time monitoring of cell proliferation under different conditions, including the presence of CDs and after their removal (washout), on the same cell population. To assess the effects of cell toxicity, the time-dependent evolution of the cell index was recorded in response to increasing CD concentrations. Each curve represents the average cell index measured in six wells. Experiments were carried out using human alveolar basal epithelial A549 adenocarcinoma cells, as a key aim of this study was to explore the potential of CDs for *in vivo* tumor imaging and therapy. Cells were seeded at 2500 cells per well and allowed to grow for several days until a cell index value close to 1 was reached, and then the culture medium was replaced with the same composition including CDs. The cells were maintained for 24 h in the presence of CDs, and then the culture medium was replaced with fresh culture medium without CDs (washout).

2.5 MRI measurements

MRI was conducted using a mouse phantom (Bioemtech, Athens, Greece) composed of a soft-tissue-mimicking material insensitive to magnetic fields. Scanning was performed at 11.7 T using an MR scanner Bruker BioSpec 117/16 USR magnet (500 MHz) associated with a sheath of gradients BGA09S HD (750 mT m^{-1}), coil RF RES 500 1H 089/072 QUAD TO AD (BMRIDE T11232V3/0047) and software version Paravision PV360.3.4MR. To get the best contrast of the T_1-weighted image, we applied a regime with a short constant echo time (TE) = 6.5 ms, and variable repetition time (TR) with a middle range sequence (364, 376, 390, 405, 423, 443, 468, 499, 541, and 606 ms). Field of view (FOV) = 60 × 30 mm (128 × 64 pixels), slice thickness = 0.6 mm, and the factor of rapid imaging with refocused echo (RARE) was 4. To get a T_2-weighted image we used a regime of constant long TR (2500 ms) and constant short TE (64 ms). FOV = 60 × 30 mm (256 × 128 pixels), slice thickness = 0.6 mm, and RARE factor = 4. Moreover, we performed MRI using another magnetic scanner with a field strength of 7 T using a Bruker BioSpec 70/20 magnet (300 MHz) associated with a sheath of gradients BGA12S2 (670 mT m^{-1}), coil RF RES 300 1H 112/072 QUAD TR M (BMRIDE T9562V3/0031) and software version Paravision PV7.0. A T_1-weighted image was obtained in a regime with a short constant echo time (TE) = 5.75 ms, and variable repetition time (TR) with a middle range sequence (28.6, 183.6, 382.9, 662.7, 1135.8, and 3500 ms). FOV = 60 × 30 mm (128 × 64 pixels), slice thickness = 1.6 mm, and RARE factor = 1. A T_2-weighted image was formed in the regime of constant long TR (2500 ms) and constant short TE (29.18 ms). FOV = 60 × 30 mm (256 × 128 pixels), slice thickness = 0.6 mm, and RARE factor = 8. These measurements were done at the PILoT facility (PILoT, INSA LYON, Bât. Léonard de Vinci, 21 Av. Jean Capelle 69621 Villeurbanne).

3. Results and discussion

3.1 Relaxometry

To use these nanomaterials as MRI contrast agents, it is crucial to evaluate the potential presence of free Gd^{3+} ions in the final dispersion and the strength of their complexation with the carbon core.[22] Free Gd^{3+} ions are known to be toxic, but their toxicity can be significantly reduced by chelating them with a suitable organic ligand or by entrapping them into a carbon skeleton.[43] The Gd^{3+} content in a sample, as well as the sample's purity and the effectiveness of Gd incorporation into the CDs, can be assessed through relaxometry by measuring the longitudinal proton relaxation time (T_1). To this end, aliquots of both filtrates and retentates from PSC and PSGd samples were collected as described in Step 8 of the production process (Fig. 1), and their T_1 values were measured (Fig. 2) to evaluate the success of the synthesis, particularly the effectiveness of the dialysis and the overall purification process. Throughout this study, PSC was used as the control, while ddH_2O served as the reference for the filtrate samples. The T_1 values of pure water remained constant at 4000 ± 20 ms, confirming the accuracy of the measurements. Following preconcentration of PSC, the relaxation time of the filtrate passing through the 3000 Da membrane was measured at 3970 ± 10 ms, closely matching that of water. However, a slight decrease in T_1 was observed in the filtrates of PSGd 0.1 and 0.5 M after preconcentration, with recorded values of 3210 ± 10 ms and 3160 ± 10 ms, respectively, compared to the reference value of 4000 ± 20 ms. This decrease may be attributed to the intrinsic paramagnetic properties of these samples, likely due to the presence of unpaired electrons in organic free radicals. Paliienko *et al.*[22] observed a similar behaviour, which they attributed to relatively stable paramagnetic organic radicals at room

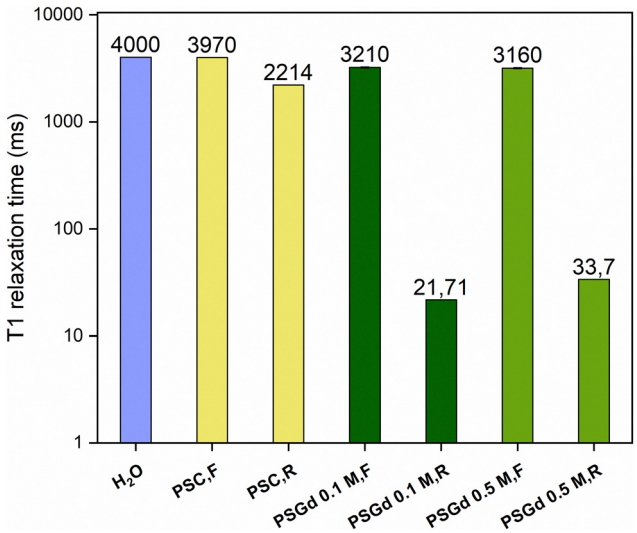

Fig. 2 T_1 relaxation time of the retentates (*R*) and filtrates (*F*) of PSC, PSGd 0.1 M and PSGd 0.5 M.

temperature. These include high-spin polymer radicals[44] and dimerized small organic radicals.[45] The preconcentration products, *i.e.* PSGd 0.1 and 0.5 M retentates, exhibited significantly reduced T_1 values of 21.71 ± 0.05 ms and 33.7 ± 0.05 ms, respectively. These findings suggest the presence of a large number of Gd-CDs with molecular weights greater than 3500 Da, which are unable to pass through the 3000 Da membrane. This also supports the conclusion that most of the Gd is incorporated into CDs with molecular weights above 3500 Da, rather than existing as free Gd^{3+} ions, which would otherwise permeate the membrane.

3.2 Physicochemical characterisation

The Gd content of CDs was determined using ICP-MS to quantify the exact concentration of Gd in PSGd 0.1 and 0.5 M samples (Table 1). The measured values, consistent with the relaxometry results, confirm successful synthesis and a relatively high Gd mass content in the PSGd 0.1 and 0.5 M retentates. In contrast, no Gd was detected in the PSC sample. Additionally, a Gd concentration of approximately 0.05 μg mL^{-1} was found in the filtrates of both Gd-doped samples, indicating an effective purification process and the absence of free Gd^{3+} ions.

The size and surface charge of the nanoparticles were analyzed at their native pH after dilution to 0.150 mg mL^{-1} in water, with the results summarized in Table 1. All samples exhibited small particle sizes (<20 nm). The PSC sample had a larger average size of about 17 nm, whereas the PSGd samples were smaller, with diameters of around 5–6 nm. The smaller size of the PSGd samples may be influenced by the limited particle growth due to the coordination of a higher amount of Gd^{3+} on the CD surface.[46] Additionally, all samples displayed a negative ζ-potential, which became progressively less negative with an increase in Gd^{3+} concentration. Notably, the PSGd 0.5 M sample demonstrated lower stability than the other two, consistent with material sedimentation observed after approximately one month of storage.

The FTIR spectra of PSC and PSGds are reported in Fig. 3A. In all spectra, the presence of the carboxyl group was confirmed by the characteristic band between 3500 and 3000 cm^{-1} due to the stretching vibration of O–H and the intense band at 1035 cm^{-1} due to the stretching vibration of C–O.[47] The band at 2926 cm^{-1} can be attributed to the stretching vibration of sp^3-hybridized alkane bonds. The band at 1580 cm^{-1} could be related either to C=N stretches in conjugated systems or to C=O bond stretching, indicating the presence of carbonyl groups on the surface of CDs. Furthermore, the band at 1384 cm^{-1} may arise from various phenomena, such as the deformation vibrations of C–H and O–H bonds in organic species, the stretching of carboxylate groups, the C–N stretching[38] or some vibrations of aromatic fragments.[22] The band at 1241 cm^{-1} could correspond to the C–O stretching of an epoxy/ether group, as reported also in our previously published paper,[48] or to the C–N vibration in amides III. While this band is clearly visible in the spectra of PSC and PSGd 0.1 M, it only appears as a shoulder in the case of PSGd 0.5 M. Moreover, it is noteworthy that the spectrum of PSGd 0.5 M shows more pronounced peaks between 1580 and 1384 cm^{-1} compared to PSC and PSGd 0.1 M, suggesting that Gd ions may be chelated by carboxyl/carboxylate groups.[49]

To further investigate the surface chemistry of the produced CDs and the coordination of Gd^{3+} ions, FTIR deconvolution was performed in the region between 1200 and 1750 cm^{-1}, where both protonated and deprotonated carboxyl groups are typically observed. Specifically, protonated groups are usually found in the region between 1650 and 1850 cm^{-1}, while the deprotonated asymmetric groups are found at around 1385 cm^{-1}.[46,50] The deconvoluted spectra are shown in Fig. S1 of the SI section. In general, a gradual decrease in the contribution of the protonated carboxyl group (Fig. S1B) at around 1725 cm^{-1} and an increase in the contribution of the deprotonated carboxyl group (Fig. S1A) at around 1370 cm^{-1} were observed with an increase in Gd concentration. This trend has recently been observed in the literature[46] and may be related to the coordination of the carboxyl groups with Gd, a phenomenon that becomes more pronounced as the Gd concentration increases.

Overall, the FTIR spectra indicate that the surface of CDs is rich in polar functional groups, such as hydroxyl, amide, and carboxyl/carboxylate moieties. These groups enhance the dispersibility of the CDs in water and other polar solvents, facilitating simpler manipulation of the samples.[38,51] These observations are consistent with the negative ζ-potential values reported in Table 1, further confirming the presence of polar functionalities introduced during the oxidation process.

The PXRD patterns of CDs are shown in Fig. 3B. All the samples display a single broad band at 30° 2θ, which is characteristic of an amorphous carbon phase.[15,52] No significant differences are observed among the three samples. These results align with the previous findings, as it is well established in the literature that CDs derived from both natural and synthetic carbon sources typically exhibit an amorphous structure.[52–55]

Transmission electron microscopy (TEM) (Fig. S2) and scanning electron microscopy (SEM) (Fig. S3) equipped with energy-dispersive X-ray spectroscopy (EDX) (Fig. S4) were employed to gain information on the morphology and the elemental composition of CDs in terms of C, O, N and Gd contents, respectively. The nanoparticles appear spherical and, in some instances, tend to form aggregates. Excluding these agglomerates, the particle sizes are consistent with the DLS results, averaging around 20 nm. The TEM image shown in Fig. S2 is representative of the PSC sample; however, no significant differences were observed when compared to the Gd-containing

Table 1 Physicochemical properties of CDs: Gd content, size, PdI and ζ-potential

Sample	μg of Gd per 1 mg of CDs	% w/w of Gd/CDs	Size[b] (nm)	PdI	ζ-potential (mV)	pH
PSC	0.0206[a]	0.00207[a]	17 ± 4	0.259	−26 ± 7	5.2
PSGd 0.1 M	2.64	0.264	6 ± 1	0.252	−13 ± 3	6.2
PSGd 0.5 M	6.20	1.91	5 ± 2	0.255	−9 ± 1	6.2

[a] Data indicate the absence of Gd. [b] Size distribution by number.

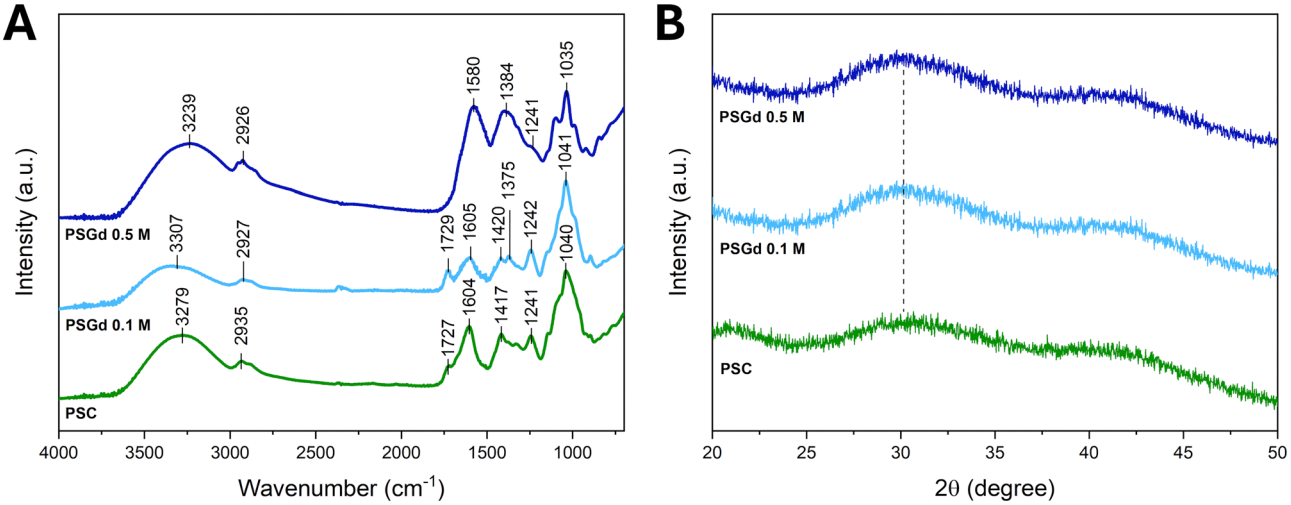

Fig. 3 FTIR spectra (A) and PXRD patterns (B) of PSC, PSGd 0.1 M and PSGd 0.5 M.

samples. It is worth noting that CDs are intrinsically difficult to image by TEM because of their small size, low atomic contrast, and high sensitivity to electron beam damage. While high-resolution TEM (HRTEM) could potentially improve image clarity, in the present case, it would not provide additional morphological information beyond that already obtained through combined TEM, PXRD, and DLS analyses.

SEM analysis revealed that the PSC sample (Fig. S3A) and the Gd-doped samples (Fig. S3B and C) exhibit an amorphous, disordered structure without a definite geometry or shape. EDX analysis confirmed the presence of C and O as the main constituent elements, along with Gd, in both doped samples. As expected, Gd was not detected in the PSC sample, consistent with the ICP-MS analysis. Additionally, the Gd content was higher in PSGd 0.5 M compared to PSGd 0.1 M, in agreement with the ICP-MS results. The C content was approximately 55–65 atomic% and the O content was around 30–35 atomic% across all samples.

3.3 Photophysical characterisation

UV-vis spectroscopy and photoluminescence were used to further characterize the samples and evaluate the optical properties of CDs. All three samples appeared brownish under daylight and exhibited blue fluorescence under UV irradiation (Fig. S5).

As reported in our previous work,[48] CDs typically exhibit one or more strong ultraviolet absorption bands between 220–270 nm and 280–350 nm. However, the exact position of these peaks can vary considerably within the UV and the visible wavelength regions, depending on both the production process and the carbon source used.[5,56] The absorption spectra shown in Fig. 4A indicate no significant differences in shape among the three samples. All spectra display a strong absorption maximum in the UV region at approximately 200 nm, along with a broad absorption band extending into the visible range.[57,58] The shoulder observed between 250 and 300 nm is attributed to the π–π* transition of C=C bonds,[55,56,58] while the broad tail in the visible range is primarily associated with transitions involving surface states, which are typically influenced by the surface functional groups.[59]

To better understand the effect of Gd^{3+} incorporation into CDs, the UV-vis spectra shown in Fig. 4A were deconvolved to elementary Gaussian-like peaks (Fig. 4B–D). After subtracting the exponential-like baselines, complex multi-component spectra were obtained, revealing clearly distinguishable deconvoluted features. Overall, the incorporation of Gd^{3+} ions leads to an increased intensity of the main absorption bands in the 2–5.5 eV range. Notably, a significant relative increase in the intensity of the peak at 4 eV – compared to those centered at 3.5 and 4.5 eV – was observed, particularly in the case of PSGd 0.5 M (Fig. 4D). According to the literature, the high energy bands (6–4.5 eV) correspond to the π → π* transitions associated with aromatic sp^2 carbons (*e.g.*, aromatic C=C bonds). In contrast, the bands between 4 and 3 eV are typically attributed to the intrinsic $n \rightarrow \pi^*$ transitions of C=O or C=N bonds within the carbon cores. The absorption feature at 2.5 eV is instead mainly influenced by surface functionalities.[60]

Excitation–emission maps of the three samples are shown in Fig. 5. All samples exhibit a main photoluminescence band with excitation in the 330–430 nm range and emission in the 350–550 nm range. The emission maximum occurs at approximately 450 nm, when the CDs are excited at around 350 nm. Compared to PSC, the PSGd 0.1 M sample shows subtle differences, including a minor band with excitation at 300 nm and emission at around 320–330 nm, as well as a very weak band with excitation at 300 nm and emission near 700 nm. In contrast, the PSGd 0.5 M sample displays significantly reduced emission intensity. As a result, the excitation–emission map also reveals the Raman scattering signal from water.[61] This diminished fluorescence is likely due to the lower colloidal stability and dispersibility of PSGd 0.5 M in water, as discussed in Section 3.2. Additionally, the high Gd content in this sample may contribute to fluorescence quenching, a phenomenon reported for various metal cations.[62–64]

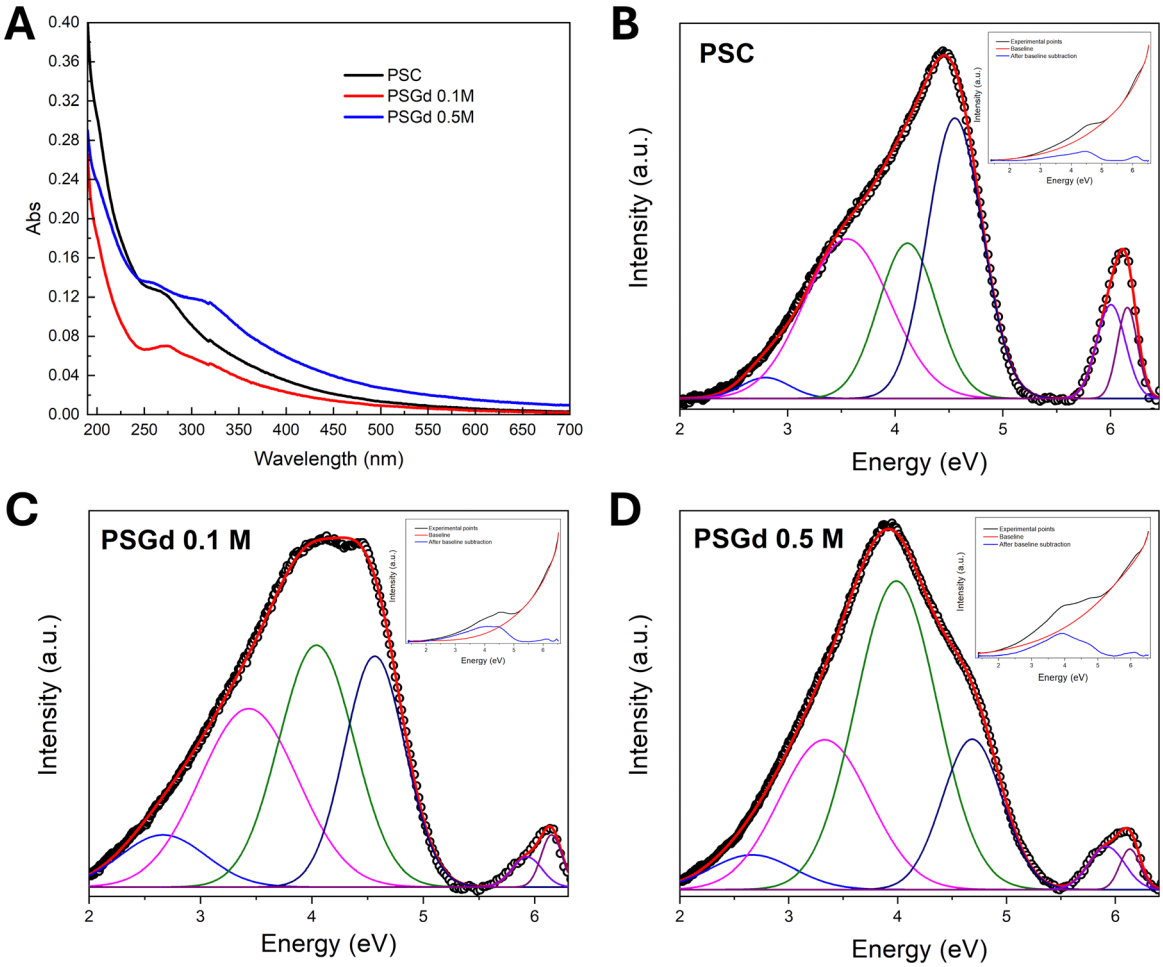

Fig. 4 Absorption spectra (A) and deconvoluted absorption spectra of PSC (B), PSGd 0.1 M (C) and PSGd 0.5 M (D).

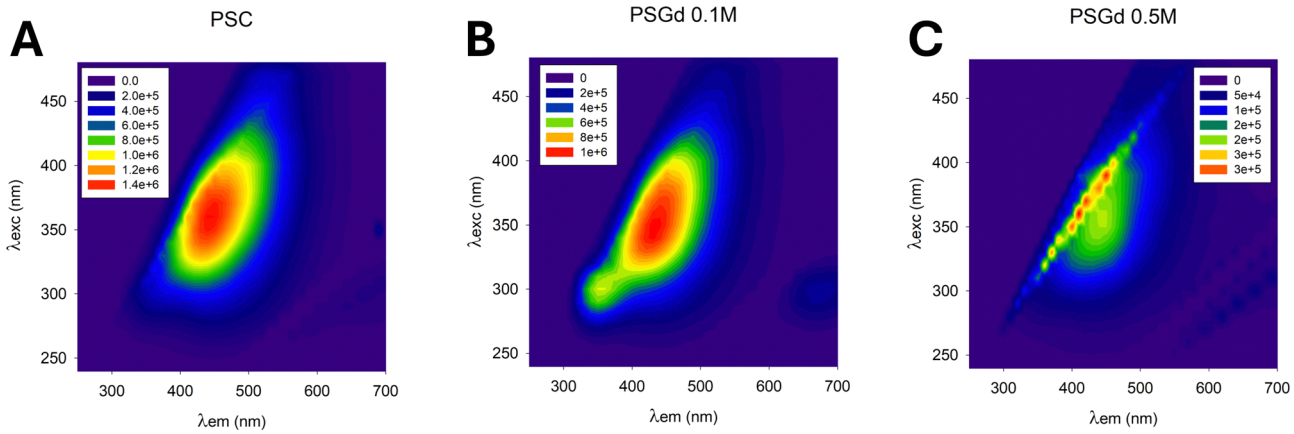

Fig. 5 Excitation–emission maps of PSC (A), PSGd 0.1 (B) and PSGd 0.5 M (C).

Quantum yields (QYs) were measured at 350 nm to compare the emission properties of the three samples. The PSC and the PSGd 0.1 M samples exhibit QYs of approximately 1%, while PSGd 0.5 M shows a significantly lower emission with a QY of 0.2%, consistent with the water Raman scattering signal visible in its excitation–emission map. It is worth noting that CDs derived from biowastes typically display lower QYs than those synthesized from high-purity chemicals. This difference is mainly attributed to the higher purity of precursors in the latter, which results in fewer structural defects and reduced non-radiative recombination sites.[65–67] To improve QY, one possible strategy involves the addition of citric acid to the

biomass precursor. Citric acid is a low-molecular-weight compound rich in carboxyl groups, which can promote the formation of well-defined carbon cores during carbonisation. These structures are believed to enhance the development of emissive centres, thereby increasing the QY.[68]

Fluorescence lifetime measurements yielded values between 2.7 and 3.3 ns for all samples, confirming their intrinsic fluorescence nature.

3.4 *In vitro* cell toxicity

Given its superior physicochemical and photophysical properties – particularly in terms of stability and emission intensity – PSGd 0.1 M was selected for biocompatibility assessment as a potential contrast agent, and its performance was compared to the control sample, PSC.

Fig. 6 shows the average normalized cell index curves, calculated from six replicates, for various CD concentrations. The cell index reflects cell viability and proliferation. As illustrated in Fig. 6A, PSC led to a concentration-dependent increase in cell index during incubation. Since values returned close to near-control values after the washout step, the observed increase suggests an enhancement in cell adhesion rather than cell proliferation. Importantly, the cells continued to proliferate after the washout, indicating that PSC is non-toxic across all tested concentrations. Conversely, Fig. 6B reveals a dose-dependent cytotoxic effect of PSGd 0.1 M. At 0.1 mg mL^{-1}, the sample shows a negligible impact on cell viability, with values similar to that of the control. At 0.25 mg mL^{-1} a slight reduction in the cell index is observed, while higher concentrations (0.5 and 1.0 mg mL^{-1}) exhibit clear cytostatic effects.

3.5 MRI assessment

PSGd 0.1 M was evaluated as a T_1-weighted MRI contrast agent using a mouse phantom model containing 9 wells (Fig. 7). Wells #1 and #2 were left unused, while wells #8 and #9 contained samples unrelated to this study (marked with a red rectangle). Well #3 contained a 3 mM $GdCl_3$ solution, chosen to match the T_1 relaxation time of PSGd 0.1 M. Well #4 contained AGuIX® (1.0 mg mL^{-1} in water), which are Gd-based polymeric nanoparticles currently in clinical trials.[69] Well #5 was filled with deionized water as the control. Wells #6 and #7 contained PSC (6.4 mg mL^{-1} in water) and PSGd 0.1 M (6.4 mg mL^{-1} in water), respectively.

MRI scans were performed using 11.7 Tesla (Fig. 7B and C) and 7 Tesla (Fig. 7D and E) scanners. Comparative Gd concentrations for each sample are provided in Table S1, with AGuIX® values sourced from the literature.[70,71] Fig. 7 shows four MRI scans with varying signal intensities and contrast. As expected,

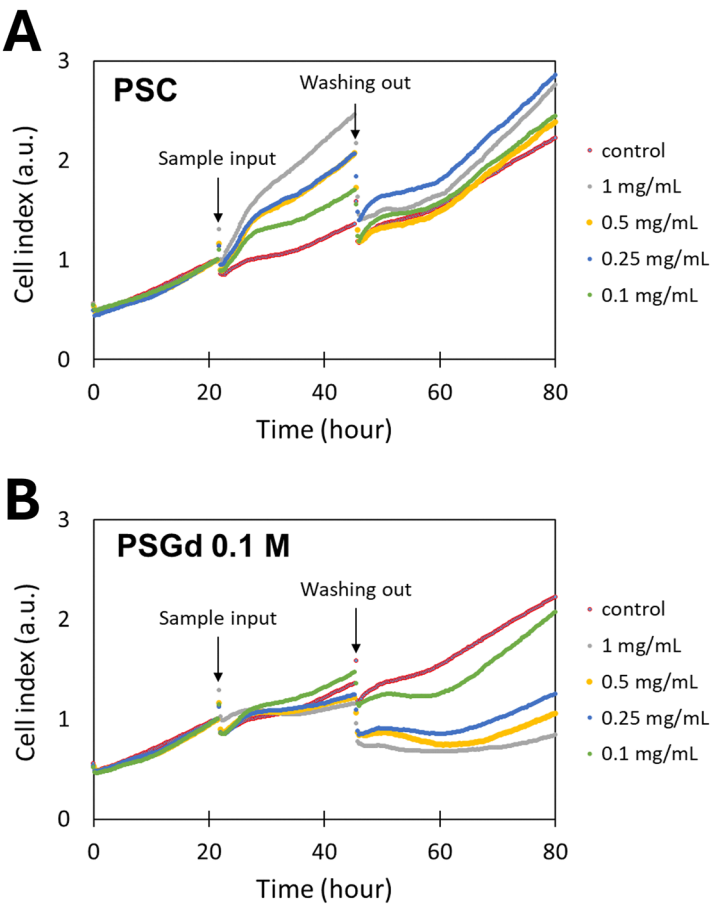

Fig. 6 Cell culture (A549) toxicity evaluation of PSC (A) and PSGd 0.1 M (B).

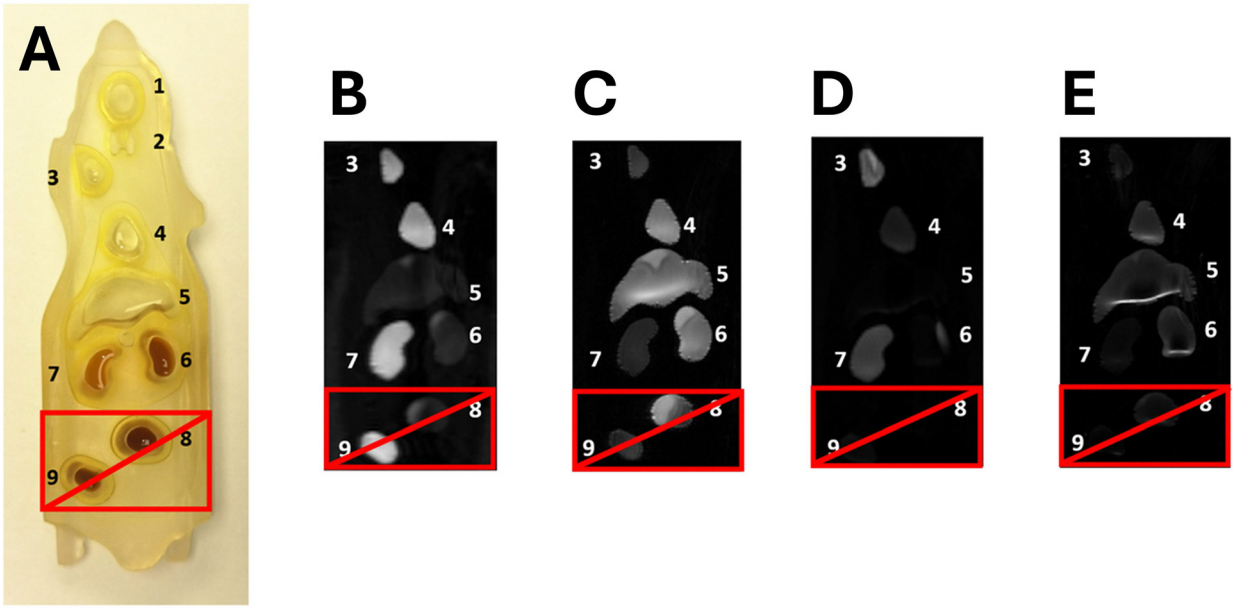

Fig. 7 Mouse phantom under room light (A), and T_1-weighted (B) and T_2-weighted (C) images acquired using an 11.7 Tesla MRI scanner, along with T_1-weighted (D) and T_2-weighted (E) images obtained with a 7 Tesla scanner. Wells were filled as follows: #1 and #2 – empty; #3 – $GdCl_3$ (3 mM), #4 – AGuIX® (1.0 mg mL^{-1}), #5 – H_2O, #6 – PSC (6.4 mg mL^{-1}), #7 – PSGd 0.1 M (6.4 mg mL^{-1}), and #8 and #9 – samples unrelated to this study (marked with a red rectangle).

the images produced with the 11.7 Tesla scans are significantly brighter than those obtained with the 7 Tesla scans, though the overall trends are consistent across both field strengths. This difference is mainly attributed to the higher signal-to-noise ratio and increased sensitivity to T_1 contrast at higher magnetic fields, which is particularly relevant for low-Gd-content formulations such as PSGd 0.1 M.

T_1-weighted images revealed high intensity (bright) regions in wells #3, #4 and #7, corresponding to $GdCl_3$, AGuIX® and PSGd 0.1 M, respectively. This confirms that PSGd 0.1 M effectively acts as a positive contrast agent, which shortens T_1 relaxation times, causing the areas where it is localized to appear bright in T_1-weighted images.[72] Notably, despite its lower Gd content (Table S1), PSGd 0.1 M produced signal intensity comparable to $GdCl_3$ and AGuIX®. Such performance at a lower Gd content is particularly advantageous from a safety perspective, as it may reduce risks associated with Gd retention without compromising image quality. The strong contrast-enhancing capabilities of PSGd 0.1 M is further emphasised by its significantly lower Gd concentration (1.08×10^{-4} mol L^{-1}) compared to clinically approved Gd-based contrast agents, such as gadoteridol, gadoterate meglumine and gadopentetate dimeglumine, which are typically formulated at a Gd concentration of 0.5 mol L^{-1} for intravenous injection in humans.[73–75] Moreover, its T_1 longitudinal relaxation time of 21.71 ± 0.05 ms at 1.4 T (60 MHz, 40 °C) is comparable to that reported for other Gd-doped CDs synthesised from coffee wastes (7.96 ms),[22] and substantially lower than the T_1 values for traditional positive contrast agents like Gd-DTPA (Magnevist®) (250–350 ms).[76] These data further support its valuable imaging performance.

The 7 Tesla scanner generated weaker signals, due to the reduced current generated by the transverse magnetization around the receiver coil at 7 Tesla compared to the 11.7 Tesla scanner.[77] As a result, in Fig. 7D, we observe less intense signals according to the Gd concentration in the samples (Table S1), with only a barely discernible area for $GdCl_3$, and practically indistinguishable signals for AGuIX® and PSGd 0.1 M. As positive contrast agents reduce the signal intensity on T_2-weighted images, negative contrast agents (*e.g.* dysprosium, ferromagnetic composites, *etc.*) are typically used.[72] The T_2-weighted images in Fig. 7C and E illustrate this phenomenon: the lower the Gd content, the brighter the observed area.

In conclusion, PSGd 0.1 M demonstrated promising MRI capabilities, especially at 11.7 Tesla. Its comparable performance to existing Gd-based contrast agents, despite its lower Gd content, highlights its potential for further development. Future studies will explore its performance at varying concentrations and validate its safety and efficacy.

3.6 Literature comparison of doped and undoped CDs

As recently reviewed by Lv *et al.*,[32] the properties of Gd-doped CDs—including size, absorption wavelength, quantum yield, and relaxation time—can vary extensively depending on the reagents and synthesis method employed. A direct comparison between biowaste-derived CDs and those produced from conventional synthetic precursors is challenging due to the different structural, optical, and surface properties arising from heterogeneous biowaste *versus* well-defined synthetic molecules.

To provide a broader context, Table 2 summarizes key parameters (particle size, quantum yield, and relaxation properties) extracted from approximately ten representative studies,

Table 2 Comparison of doped and undoped CDs reported in the literature, highlighting key physicochemical and imaging properties

Precursor/source	Doping	Size (nm)	QY (%)	T_1 (ms) and r_1 (mM^{-1} s^{-1})	Reported application	Ref.
Peanut shells	Gd-doped	5–7	1.0	21.7 ms [1.4 T]	MRI	This work
Coffee waste	Gd-doped	2–7	n.d.	7.96 ms [1.4 T]	MRI	22
Citric acid, $GdCl_3$	Gd-doped	50–100	4.06	22.31 ms [0.5 T]/ 14.08 mM^{-1} s^{-1}	FI/MRI	49
Sucrose, $GdCl_3$	Gd-doped	~5	5.4	11.36 mM^{-1} s^{-1}	MRI/optical nanoprobes	78
Na_2EDTA, $GdCl_3$, $YbCl_3$, L-arginine	Gd- and Yb-doped	5–6	16.84	6.65 mM^{-1} s^{-1}	FI/MRI/CT	79
DPH[a], $MnCl_2$	Mn-doped	40–200	28.30	0.932 mM^{-1} s^{-1}	FI/MRI	80
$Mn(CH_3COO)_2$, *o*-phenylenediamine	Mn-doped	~5	9.57	12.69 mM^{-1} s^{-1}	FI/MRI	81
Peanut shells	Undoped	13–21	1.0	2214 ms [1.4 T]	Control sample in MRI	This work
Coffee waste	Undoped	4–11	n.d.	2030 ms [1.4 T]	Control sample in MRI	22
Citric acid, ethylene diamine	Undoped	~4	53	n.d.	FI	82
Lemon juice, ethanol	Undoped	~5	28	n.d.	FI	83

[a] DPH: 5,5′-diphenylhydantoin.

comparing our doped and undoped CDs with a wide range of reported systems used for bioimaging purposes, including fluorescence imaging (FI), MRI and X-ray computed tomography (CT). The size of reported CDs generally ranges from 2 to 20 nm, including those of this study, whereas only samples from ref. 49 and 80 reached up to 200 nm, likely due to aggregation. Undoped CDs typically exhibit long T_1 relaxation times, precluding their use as MRI contrast agents despite often high photoluminescence quantum yields, particularly when derived from synthetic precursors. In contrast, doped CDs, including PSGd 0.1 M, display T_1 values in the low millisecond range (7–22 ms) and high r_1 relaxivities (up to approximately 15 mM^{-1} s^{-1}), confirming their suitability as MRI contrast agents.

Analysis of Table 2 shows that biowaste-derived doped CDs achieve MRI performance comparable to conventional synthetic CDs. The r_1 relaxivity of PSGd 0.1 M is comparable to or higher than many Gd-doped CDs from chemical precursors. Although undoped CDs often show higher photoluminescence quantum yields, their long T_1 values preclude MRI applications, highlighting the essential role of metal doping. Trends in size, quantum yield, and relaxation properties across different precursors further demonstrate that co-doping with metals such as Gd, Yb, or Mn is key to enabling multi-modal imaging capabilities, including fluorescence, MRI, and CT.

4. Conclusion

Fluorescent Gd-doped CDs were successfully synthesised from peanut shells using a microwave-assisted method, representing a sustainable approach in line with the principles of circular economy. The preparation is simple and potentially scalable, although the dialysis purification step could be replaced with more efficient and reproducible systems, such as tangential flow filtration (TFF) or other membrane-based purification techniques, to facilitate industrial applications. Gd incorporation was confirmed by a significant decrease in longitudinal proton relaxation time (T_1) compared to controls, indicating effective integration into the CD structure. The resulting CDs exhibited surface-rich polar functional groups—such as hydroxyl, amide, and carboxyl/carboxylate moieties—facilitating high dispersibility in water and polar solvents and thus enabling easier manipulation. Importantly, Gd-doped CDs showed no cytotoxicity towards human A549 adenocarcinoma cells up to 0.1 mg mL^{-1} and demonstrated substantial contrast enhancement, especially under an 11.7 Tesla MRI scanner in a mouse phantom model.

While conventional synthesis from chemical precursors allows for precise tuning of optical and physicochemical properties, biowaste-based methods emphasize sustainability and biocompatibility, often sacrificing fine control over material parameters. These intrinsic differences highlight the unique value and potential of biowaste-derived CDs, while also indicating that more studies and comprehensive reports are needed to fully evaluate and benchmark their performance. Looking ahead, these CDs could be functionalized with targeting ligands such as hyaluronic acid or folic acid, which bind to CD44 and folate receptors, respectively—both commonly overexpressed in a variety of cancers—opening the way for cell-specific imaging and therapeutic applications.[84,85]

Author contributions

Conceptualization: M. I. and V. L.; data curation: F. M., A. M., and K. P.; formal analysis: F. M. and A. M.; funding acquisition: M. I. and V. L.; investigation: F. M., A. M., K. P., and A. G.; methodology: F. M., K. P., V. L., and A. A.; supervision: M. I., M. M., and V. L.; writing – original draft: F. M.; writing – review and editing: all authors.

Conflicts of interest

There are no conflicts to declare.

Data availability

The datasets supporting the findings of this study are available from the corresponding author upon request. All relevant experimental data, including characterization files, imaging

results, and supplementary figures, are provided within the article and its SI. See DOI: https://doi.org/10.1039/d5tb01420d.

Acknowledgements

This work was supported by the EU Horizon 2020 Research and Innovation Staff Exchange Programme (RISE) under the Marie Skłodowska-Curie Action (H2020-MSCA-RISE-2020, project 101008159 "UNAT").

References

1 S. Geisendorf and F. Pietrulla, The Circular Economy and Circular Economic Concepts—a Literature Analysis and Redefinition, *Thunderbird Int. Bus. Rev.*, 2018, **60**(5), 771–782, DOI: 10.1002/tie.21924.
2 Circular economy: definition, importance and benefits | Topics | European Parliament. https://www.europarl.europa.eu/topics/en/article/20151201STO05603/circular-economy-definition-importance-and-benefits (accessed 2024-03-19).
3 Environment Agency, G. 9 Principles for a Circular Economy.
4 S. D. R. Lugo, K. Kimita and N. Nishino, Circular Food Economy Framework: Challenges and Initiatives, *Procedia CIRP*, 2022, **112**, 28–33, DOI: 10.1016/j.procir.2022.09.019.
5 C. Kang, Y. Huang, H. Yang, X. F. Yan and Z. P. Chen, A Review of Carbon Dots Produced from Biomass Wastes, *Nanomaterials*, 2020, **10**(11), 1–24, DOI: 10.3390/nano10112316.
6 H. Salimi Shahraki, A. Ahmad and R. Bushra, Green Carbon Dots with Multifaceted Applications– Waste to Wealth Strategy, *FlatChem*, 2022, **31**, 100310, DOI: 10.1016/J.FLATC.2021.100310.
7 P. Zhu, S. Wang, Y. Zhang, Y. Li, Y. Liu, W. Li, Y. Wang, X. Yan and D. Luo, Carbon Dots in Biomedicine: A Review, *ACS Appl. Bio Mater.*, 2022, **5**(5), 2031–2045, DOI: 10.1021/acsabm.1c01215.
8 P. Kaur and G. Verma, Converting Fruit Waste into Carbon Dots for Bioimaging Applications, *Mater. Today Sustainability*, 2022, **18**, 100137, DOI: 10.1016/j.mtsust.2022.100137.
9 Y. Song, S. Zhu and B. Yang, Bioimaging Based on Fluorescent Carbon Dots, *RSC Adv.*, 2014, **4**(52), 27184, DOI: 10.1039/c3ra47994c.
10 L. Li, C. Lu, S. Li, S. Liu, L. Wang, W. Cai, W. Xu, X. Yang, Y. Liu and R. Zhang, A High-Yield and Versatile Method for the Synthesis of Carbon Dots for Bioimaging Applications, *J. Mater. Chem. B*, 2017, **5**(10), 1935–1942, DOI: 10.1039/C6TB03003C.
11 H. Li, X. Yan, D. Kong, R. Jin, C. Sun, D. Du, Y. Lin and G. Lu, Recent Advances in Carbon Dots for Bioimaging Applications, *Nanoscale Horiz.*, 2020, **5**(2), 218–234, DOI: 10.1039/C9NH00476A.
12 Y. Newman Monday, J. Abdullah, N. A. Yusof, S. Abdul Rashid and R. H. Shueb, Facile Hydrothermal and Solvothermal Synthesis and Characterization of Nitrogen-Doped Carbon Dots from Palm Kernel Shell Precursor, *Appl. Sci.*, 2021, **11**(4), 1630, DOI: 10.3390/app11041630.
13 H. K. M. Ng, G. K. Lim and C. P. Leo, Comparison between Hydrothermal and Microwave-Assisted Synthesis of Carbon Dots from Biowaste and Chemical for Heavy Metal Detection: A Review, *Microchem. J.*, 2021, **165**, 106116, DOI: 10.1016/j.microc.2021.106116.
14 J. Zhou, Z. Sheng, H. Han, M. Zou and C. Li, Facile Synthesis of Fluorescent Carbon Dots Using Watermelon Peel as a Carbon Source, *Mater. Lett.*, 2012, **66**(1), 222–224, DOI: 10.1016/j.matlet.2011.08.081.
15 A. Prasannan and T. Imae, One-Pot Synthesis of Fluorescent Carbon Dots from Orange Waste Peels, *Ind. Eng. Chem. Res.*, 2013, **52**(44), 15673–15678, DOI: 10.1021/ie402421s.
16 R. Bandi, B. R. Gangapuram, R. Dadigala, R. Eslavath, S. S. Singh and V. Guttena, Facile and Green Synthesis of Fluorescent Carbon Dots from Onion Waste and Their Potential Applications as Sensor and Multicolour Imaging Agents, *RSC Adv.*, 2016, **6**(34), 28633–28639, DOI: 10.1039/c6ra01669c.
17 A. Dager, T. Uchida, T. Maekawa and M. Tachibana, Synthesis and Characterization of Mono-Disperse Carbon Quantum Dots from Fennel Seeds: Photoluminescence Analysis Using Machine Learning, *Sci. Rep.*, 2019, **9**(1), 1–10, DOI: 10.1038/s41598-019-50397-5.
18 S. Caspani, R. Magalhães, J. P. Araújo and C. T. Sousa, Magnetic Nanomaterials as Contrast Agents for MRI, *Materials*, 2020, **13**(11), 2586, DOI: 10.3390/ma13112586.
19 A. D. Sherry and M. Woods, Chemical exchange saturation transfer contrast agents for magnetic resonance imaging, *Annu. Rev. Biomed. Eng.*, 2008, **10**, 391–411, DOI: 10.1146/annurev.bioeng.9.060906.151929.
20 D. Hao, T. Ai, F. Goerner, X. Hu, V. M. Runge and M. Tweedle, Review: MR Physics for Clinicians. MRI Contrast Agents: Basic Chemistry and Safety, *J. Magn. Reson. Imaging*, 2012, **1071**, 1060–1071, DOI: 10.1002/jmri.23725.
21 M. M. R. Bellin, Contrast Agents, the Old and the New, *Eur. J. Radiol.*, 2006, **60**, 314–323, DOI: 10.1016/j.ejrad.2006.06.021.
22 K. Paliienko, A. Topchylo, S. Alekseev, A. Géloën, Y. Milovanov, T. Lysenko, V. Skryshevsky, T. Borisova and V. Lysenko, Green Synthesis of Biocompatible Gd3 + -Doped Ultrasmall Carbon-Based Nanohybrids from Coffee Wastes, *Carbon Resour. Convers.*, 2024, **7**, 100197, DOI: 10.1016/j.crcon.2023.09.001.
23 X. Mao, J. Xu and H. Cui, Functional Nanoparticles for Magnetic Resonance Imaging, *Wiley Interdiscip. Rev.: Nanomed. Nanobiotechnol.*, 2016, **8**(6), 814–841, DOI: 10.1002/wnan.1400.
24 G. W. Kajjumba, M. Attene-Ramos and E. J. Marti, Toxicity of Lanthanide Coagulants Assessed Using Four in Vitro Bioassays, *Sci. Total Environ*, 2021, **800**, 149556, DOI: 10.1016/j.scitotenv.2021.149556.
25 Y. T. Lin, R. X. Liu, G. Audira, M. E. Suryanto, M. J. M. Roldan, J. S. Lee, T. R. Ger and C. D. Hsiao, Lanthanides toxicity in zebrafish embryos are correlated to their atomic number, *Toxics*, 2022, **10**(6), 336, DOI: 10.3390/toxics10060336.

26 D. K. Ji, G. Reina, H. Liang, D. Zhang, S. Guo, B. Ballesteros, C. Ménard-Moyon, J. Li and A. Bianco, Gadolinium-Incorporated Carbon Nanodots for T1-Weighted Magnetic Resonance Imaging, *ACS Appl. Nano Mater.*, 2021, **4**, 1467, DOI: 10.1021/acsanm.0c02993.

27 M. Jiao, Y. Wang, W. Wang, X. Zhou, J. Xu, Y. Xing, L. Chen, Y. Zhang, M. Chen, K. Xu and S. Zheng, Gadolinium Doped Red-Emissive Carbon Dots as Targeted Theranostic Agents for Fluorescence and MR Imaging Guided Cancer Phototherapy, *Chem. Eng. J.*, 2022, **440**, 135965, DOI: 10.1016/j.cej.2022.135965.

28 M. J. Molaei, Gadolinium - Doped Fluorescent Carbon Quantum Dots as MRI Contrast Agents and Fluorescent Probes, *Sci. Rep.*, 2022, 1–11, DOI: 10.1038/s41598-022-22518-0.

29 P. Eriksson, A. H. T. Truong, C. Brommesson, A. du Rietz, G. R. Kokil, R. D. Boyd, Z. Hu, T. T. Dang, P. O. A. Persson and K. Uvdal, Cerium Oxide Nanoparticles with Entrapped Gadolinium for High T_1 Relaxivity and ROS-Scavenging Purposes, *ACS Omega*, 2022, **7**(24), 21337–21345, DOI: 10.1021/acsomega.2c03055.

30 W. Hou, F. Xia, G. Alfranca, H. Yan, X. Zhi, Y. Liu, C. Peng, C. Zhang, J. M. de la Fuente and D. Cui, Nanoparticles for Multi-Modality Cancer Diagnosis: Simple Protocol for Self-Assembly of Gold Nanoclusters Mediated by Gadolinium Ions, *Biomaterials*, 2017, **120**, 103–114, DOI: 10.1016/j.biomaterials.2016.12.027.

31 M. Cao, P. Wang, Y. Kou, J. Wang, J. Liu, Y. Li, J. Li, L. Wang and C. Chen, Gadolinium(III)-Chelated Silica Nanospheres Integrating Chemotherapy and Photothermal Therapy for Cancer Treatment and Magnetic Resonance Imaging, *ACS Appl. Mater. Interfaces*, 2015, **7**(45), 25014–25023, DOI: 10.1021/acsami.5b06938.

32 X. Lv, L. Chen, R. Guo, Y. Yang, X. Liu and S. Yu, Gadolinium Functionalized Carbon Dot Complexes for Dual-Modal Imaging: Structure, Performance, and Applications, *ACS Biomater. Sci. Eng.*, 2025, **11**, 2037–2051, DOI: 10.1021/acsbiomaterials.4c02278.

33 J. Du, S. Zhou, Y. Ma, Y. Wei, Q. Li, H. Huang, L. Chen, Y. Yang and S. Yu, Folic Acid Functionalized Gadolinium-Doped Carbon Dots as Fluorescence/Magnetic Resonance Imaging Contrast Agent for Targeted Imaging of Liver Cancer, *Colloids Surf., B*, 2024, **234**, 113721, DOI: 10.1016/j.colsurfb.2023.113721.

34 L. Ansari, S. Hallaj, T. Hallaj and M. Amjadi, Doped-Carbon Dots: Recent Advances in Their Biosensing, Bioimaging and Therapy Applications, *Colloids Surf., B*, 2021, **203**, 111743, DOI: 10.1016/j.colsurfb.2021.111743.

35 L. Wang, W. Zhou, D. Yang, H. Zhe, S. Mei, J. Yuan, W. Zhang, H. Li, H. Fan, F. Xie and R. Guo, Gadolinium-Doped Carbon Dots with High-Performance in Dual-Modal Molecular Imaging, *Anal. Methods*, 2021, **13**(21), 2442–2449, DOI: 10.1039/D1AY00270H.

36 C. Yu, T. Xuan, Y. Chen, Z. Zhao, X. Liu, G. Lian and H. Li, Gadolinium-Doped Carbon Dots with High Quantum Yield as an Effective Fluorescence and Magnetic Resonance Bimodal Imaging Probe, *J. Alloys Compd.*, 2016, **688**, 611–619, DOI: 10.1016/j.jallcom.2016.07.226.

37 D. Li, P. Jing, L. Sun, Y. An, X. Shan, X. Lu, D. Zhou, D. Han, D. Shen, Y. Zhai, S. Qu, R. Zbořil and A. L. Rogach, Near-Infrared Excitation/Emission and Multiphoton-Induced Fluorescence of Carbon Dots, *Adv. Mater.*, 2018, **30**(13), 1705913, DOI: 10.1002/adma.201705913.

38 N. Mauro, R. Cillari, C. Gagliardo, M. A. Utzeri and M. Marrale, Gadolinium-Doped Carbon Nanodots as Potential Anticancer Tools for Multimodal Image-Guided Photothermal Therapy and Tumor Monitoring, *ACS Appl. Nano Mater.*, 2023, **6**(18), 17206–17217, DOI: 10.1021/acsanm.3c03583.

39 Y.-Y. Yao, G. Gedda, W. M. Girma, C.-L. Yen, Y.-C. Ling and J.-Y. Chang, Magnetofluorescent Carbon Dots Derived from Crab Shell for Targeted Dual-Modality Bioimaging and Drug Delivery, *ACS Appl. Mater. Interfaces*, 2017, **9**(16), 13887–13899, DOI: 10.1021/acsami.7b01599.

40 M. C. Echeverria and M. Nuti, Valorisation of the Residues of Coffee Agro-Industry: Perspectives and Limitations, *Open Waste Manage. J.*, 2017, **10**(1), 13–22, DOI: 10.2174/1874400201710010013.

41 R. Kumar Gupta, E. AE Ali, F. Abd El Gawad, V. Mecheal Daood, H. Sabry, S. Karunanithi and P. Prakash Srivastav, Valorization of Fruits and Vegetables Waste Byproducts for Development of Sustainable Food Packaging Applications, *Waste Manage. Bulletin.*, 2024, **2**(4), 21–40, DOI: 10.1016/j.wmb.2024.08.005.

42 X. Ma and H. Tian, Photochemistry and Photophysics. Concepts, Research, Applications. By Vincenzo Balzani, Paola Ceroni and Alberto Juris, *Angew. Chem., Int. Ed.*, 2014, **53**(34), 8817, DOI: 10.1002/anie.201405219.

43 H. Ersoy and F. J. Rybicki, Biochemical Safety Profiles of Gadolinium-Based Extracellular Contrast Agents and Nephrogenic Systemic Fibrosis, *J. Magn. Reson. Imaging*, 2007, **1197**, 1190–1197, DOI: 10.1002/jmri.21135.

44 B. M. Weckhuysen, R. Ramachandra Rao, J. Pelgrims, R. A. Schoonheydt, P. Bodart, G. Debras, O. Collart, P. Van Der Voort and E. F. Vansant, Synthesis, Spectroscopy and Catalysis of [Cr(Acac)3] Complexes Grafted onto MCM-41 Materials: Formation of Polyethylene Nanofibres within Mesoporous Crystalline Aluminosilicates, *Chem. – Eur. J.*, 2000, **6**(16), 2960–2970, DOI: 10.1002/1521-3765(20000818)6:16<2960::AID-CHEM2960>3.0.CO;2-7.

45 W. Fujita and K. Awaga, Room-Temperature Magnetic Bistability in Organic Radical Crystals, *Science*, 1999, **286**(5438), 261–262, DOI: 10.1126/science.286.5438.261.

46 N. Mitiushev, D. U. Musaeva, D. A. Artemov, A. V. Syuy, O. S. Pavlova, Y. A. Pirogov, E. Kabachkov, A. Fionov, V. G. Kytin, E. Konstantinova, V. Y. Timoshenko and A. N. Baranov, Gadolinium-Doped Carbon Nanoparticles: Coordination, Spectroscopic Characterization and Magnetic Resonance Relaxivity, *Dalton Trans.*, 2025, **54**, 7340, DOI: 10.1039/D5DT00362H.

47 A. Kurdekar, L. A. A. Chunduri, E. P. Bulagonda, M. K. Haleyurgirisetty, V. Kamisetti and I. K. Hewlett, Comparative Performance Evaluation of Carbon Dot-Based Paper Immunoassay on Whatman Filter Paper and Nitrocellulose

Paper in the Detection of HIV Infection, *Microfluid. Nanofluid.*, 2016, **20**, 99, DOI: 10.1007/s10404-016-1763-9.

48 F. Mancini, A. Menichetti, L. D. Esposti, M. Montesi, S. Panseri, G. Bassi, M. Montalti, L. Lazzarini, A. Adamiano and M. Iafisco, Fluorescent Carbon Dots from Food Industry By-Products for Cell Imaging, *J. Funct. Biomater.*, 2023, **14**(2), 90, DOI: 10.3390/jfb14020090.

49 H. Liao, Z. Wang, S. Chen, H. Wu, X. Ma and M. Tan, One-Pot Synthesis of Gadolinium-Doped Carbon Dots for Fluorescence/Magnetic Resonance Bimodal Imaging, *RSC Adv.*, 2015, **5**(82), 66575–66581, DOI: 10.1039/C5RA09948J.

50 K. Saito, T. Xu and H. Ishikita, Correlation between C═O Stretching Vibrational Frequency and PKa Shift of Carboxylic Acids, *J. Phys. Chem. B*, 2022, **126**(27), 4999–5006, DOI: 10.1021/acs.jpcb.2c02193.

51 W. Liu, C. Li, Y. Ren, X. Sun, W. Pan, Y. Li, J. Wang and W. Wang, Carbon Dots: Surface Engineering and Applications, *J. Mater. Chem. B*, 2016, **4**, 5772–5788, DOI: 10.1039/c6tb00976j.

52 M. Xue, Z. Zhan, M. Zou, L. Zhang and S. Zhao, Green Synthesis of Stable and Biocompatible Fluorescent Carbon Dots from Peanut Shells for Multicolor Living Cell Imaging, *New J. Chem.*, 2016, **40**(2), 1698–1703, DOI: 10.1039/c5nj02181b.

53 G. Chen, S. Wu, L. Hui, Y. Zhao, J. Ye, Z. Tan, W. Zeng, Z. Tao, L. Yang and Y. Zhu, Assembling Carbon Quantum Dots to a Layered Carbon for High-Density Supercapacitor Electrodes, *Sci. Rep.*, 2016, **6**, 1–9, DOI: 10.1038/srep19028.

54 Y. Dong, L. Wan, J. Cai, Q. Fang, Y. Chi and G. Chen, Natural Carbon-Based Dots from Humic Substances, *Sci. Rep.*, 2015, **5**, 1–8, DOI: 10.1038/srep10037.

55 Y. Zhao, Y. Zhang, X. Liu, H. Kong, Y. Wang, G. Qin, P. Cao, X. Song, X. Yan, Q. Wang and H. Qu, Novel Carbon Quantum Dots from Egg Yolk Oil and Their Haemostatic Effects, *Sci. Rep.*, 2017, **7**(1), 1–8, DOI: 10.1038/s41598-017-04073-1.

56 W. U. Khan, D. Wang, W. Zhang, Z. Tang, X. Ma, X. Ding, S. Du and Y. Wang, High Quantum Yield Green-Emitting Carbon Dots for Fe(III) Detection, Biocompatible Fluorescent Ink and Cellular Imaging, *Sci. Rep.*, 2017, **7**(1), 1–9, DOI: 10.1038/s41598-017-15054-9.

57 S. N. Baker and G. A. Baker, Luminescent Carbon Nanodots: Emergent Nanolights, *Angew. Chem., Int. Ed.*, 2010, **49**(38), 6726–6744, DOI: 10.1002/anie.200906623.

58 K. Suzuki, L. Malfatti, M. Takahashi, D. Carboni, F. Messina, Y. Tokudome, M. Takemoto and P. Innocenzi, Design of Carbon Dots Photoluminescence through Organo-Functional Silane Grafting for Solid-State Emitting Devices, *Sci. Rep.*, 2017, **7**(1), 1–11, DOI: 10.1038/s41598-017-05540-5.

59 H. Ding, S. B. Yu, J. S. Wei and H. M. Xiong, Full-Color Light-Emitting Carbon Dots with a Surface-State-Controlled Luminescence Mechanism, *ACS Nano*, 2016, **10**(1), 484–491, DOI: 10.1021/acsnano.5b05406.

60 L. M. Amzel, D. F. Covey, C. Fenselau, A. Nickon and C. H. Robinson, Organic Structural Analysis, *Biol. Mass Spectrom.*, 1977, **4**(6), vii–ix, DOI: 10.1002/bms.1200040612.

61 A. Kalita, K. Deka and M. P. C. Kalita, On the Influence of Raman Scattering of Water in the Photoluminescence Measurement of Water Dispersed ZnO Nanocrystals, *Methods Appl. Fluoresc.*, 2017, **5**(2), 027001, DOI: 10.1088/2050-6120/aa6ab8.

62 B. Wang, H. Cai, G. I. N. Waterhouse, X. Qu, B. Yang and S. Lu, Carbon Dots in Bioimaging, Biosensing and Therapeutics: A Comprehensive Review, *Small Sci.*, 2022, **2**, 2200012, DOI: 10.1002/smsc.202200012.

63 F. Ehrat, S. Bhattacharyya, J. Schneider, A. Lo, R. Wyrwich, A. L. Rogach, J. K. Stolarczyk, A. S. Urban and J. Feldmann, Tracking the Source of Carbon Dot Photoluminescence: Aromatic Domains versus Molecular Fluorophores, *Nano Lett.*, 2017, **17**(12), 7710–7716, DOI: 10.1021/acs.nanolett.7b03863.

64 Y. Han, L. Shi, X. Luo, X. Chen, W. Yang, W. Tang, J. Wang, T. Yue and Z. Li, A Signal-on Fl Uorescent Sensor for Ultra-Trace Detection of Hg^{2+} via Ag^{+} Mediated Sulfhydryl Functionalized Carbon Dots, *Carbon*, 2019, **149**, 355–363, DOI: 10.1016/j.carbon.2019.04.052.

65 V. Ramanan, S. K. Thiyagarajan, K. Raji, R. Suresh, R. Sekar and P. Ramamurthy, Outright Green Synthesis of Fluorescent Carbon Dots from Eutrophic Algal Blooms for In Vitro Imaging, *ACS Sustainable Chem. Eng.*, 2016, **4**(9), 4724–4731, DOI: 10.1021/acssuschemeng.6b00935.

66 H. Ding, J. Wei, P. Zhang, Z. Zhou, Q. Gao and H. Xiong, Solvent-Controlled Synthesis of Highly Luminescent Carbon Dots with a Wide Color Gamut and Narrowed Emission Peak Widths, *Small*, 2018, **14**, 1800612, DOI: 10.1002/smll.201800612.

67 C. Cheng, M. Xing and Q. Wu, A Universal Facile Synthesis of Nitrogen and Sulfur Co-Doped Carbon Dots from Cellulose-Based Biowaste for Fluorescent Detection of Fe3+ Ions and Intracellular Bioimaging, *Mater. Sci. Eng., C*, 2019, **99**, 611–619, DOI: 10.1016/j.msec.2019.02.003.

68 X. Li, X. Liu, Y. Su, T. Jiang, D. Li and X. Ma, Green Synthesis of Carbon Quantum Dots from Wasted Enzymatic Hydrolysis Lignin Catalyzed by Organic Acids for UV Shielding and Antioxidant Fluorescent Flexible Film, *Ind. Crops Prod.*, 2022, **188**, 115568, DOI: 10.1016/j.indcrop.2022.115568.

69 E. Thivat, M. Casile, J. Moreau, I. Molnar, S. Dufort, K. Seddik, G. Le Duc, O. De Beaumont, M. Loeffler, X. Durando and J. Biau, Phase I/II Study Testing the Combination of AGuIX Nanoparticles with Radiochemotherapy and Concomitant Temozolomide in Patients with Newly Diagnosed Glioblastoma (NANO-GBM Trial Protocol), *BMC Cancer*, 2023, **23**(1), 344, DOI: 10.1186/s12885-023-10829-y.

70 P. Mowat, A. Mignot, W. Rima, F. Lux, O. Tillement, C. Roulin, M. Dutreix, D. Bechet, S. Huger, L. Humbert, M. Barberi-Heyob, M. T. Aloy, E. Armandy, C. Rodriguez-Lafrasse, G. Le Duc, S. Roux and P. Perriat, Radiosensitizing Effects of Ultrasmall Gadolinium Based Particles on Tumour Cells, *J. Nanosci. Nanotechnol.*, 2011, **11**(9), 7833–7839, DOI: 10.1166/jnn.2011.4725.

71 T. Borisova, N. Pozdnyakova, N. Krisanova, A. Pastukhov, M. Dudarenko, K. Paliienko, V. Grytsaenko, F. Lux, V. Lysenko, P. Rocchi, S. Komisarenko and O. Tillement,

Unique Features of Brain Metastases-Targeted AGuIX Nanoparticles vs Their Constituents: A Focus on Glutamate-/GABA-Ergic Neurotransmission in Cortex Nerve Terminals, *Food Chem. Toxicol.*, 2021, **149**, 112004, DOI: **10.1016/j.fct.2021.112004**.

72 Y.-D. Xiao, R. Paudel, J. Liu, C. Ma, Z.-S. Zhang and S.-K. Zhou, MRI Contrast Agents: Classification and Application, *Int. J. Mol. Med.*, 2016, **38**(5), 1319–1326, DOI: **10.3892/ijmm.2016.2744**.

73 S. Aime and P. Caravan, Biodistribution of Gadolinium-based Contrast Agents, Including Gadolinium Deposition, *J. Magn. Reson. Imaging*, 2009, **30**(6), 1259–1267, DOI: **10.1002/jmri.21969**.

74 F. Iacobellis, M. Di Serafino, C. Russo, R. Ronza, M. Caruso, G. Dell'Aversano Orabona, C. Camillo, V. Sabatino, D. Grimaldi, C. Rinaldo, L. Barbuto, F. Verde, G. Giacobbe, M. L. Schillirò, E. Scarano and L. Romano, Safe and Informed Use of Gadolinium-Based Contrast Agent in Body Magnetic Resonance Imaging: Where We Were and Where We Are, *Jpn. Clin. Med.*, 2024, **13**(8), 2193, DOI: **10.3390/jcm13082193**.

75 S. Fujita, M. Nakazawa, A. Hagiwara, R. Ueda, M. Horita, T. Maekawa, R. Irie, C. Andica, K. Kunishima Kumamaru, M. Hori and S. Aoki, Estimation of Gadolinium-Based Contrast Agent Concentration Using Quantitative Synthetic MRI and Its Application to Brain Metastases: A Feasibility Study, *Magn. Reson. Med. Sci.*, 2019, **18**(4), 260–264, DOI: **10.2463/mrms.mp.2018-0119**.

76 P. Doeblin, R. Schilling, M. Wagner, R. Luhur, A. Huppertz, B. Hamm, M. Taupitz and T. Durmus, Intraindividual Comparison of T1 Relaxation Times after Gadobutrol and Gd-DTPA Administration for Cardiac Late Enhancement Imaging, *Eur. J. Radiol.*, 2014, **83**(4), 660–664, DOI: **10.1016/j.ejrad.2013.12.019**.

77 R. Bitar, G. Leung, R. Perng, S. Tadros, A. R. Moody, J. Sarrazin, C. McGregor, M. Christakis, S. Symons, A. Nelson and T. P. Roberts, MR Pulse Sequences: What Every Radiologist Wants to Know but Is Afraid to Ask, *RadioGraphics*, 2006, **26**(2), 513–537, DOI: **10.1148/rg.262055063**.

78 N. Gong, H. Wang, S. Li, Y. Deng, X. Chen, L. Ye and W. Gu, Microwave-Assisted Polyol Synthesis of Gadolinium-Doped Green Luminescent Carbon Dots as a Bimodal Nanoprobe, *Langmuir*, 2014, **30**(36), 10933–10939, DOI: **10.1021/la502705g**.

79 Y. Zhao, X. Hao, W. Lu, R. Wang, X. Shan, Q. Chen, G. Sun and J. Liu, Facile Preparation of Double Rare Earth-Doped Carbon Dots for MRI/CT/FI Multimodal Imaging, *ACS Appl. Nano Mater.*, 2018, **1**(6), 2544–2551, DOI: **10.1021/acsanm.8b00137**.

80 C. S. Stan, A. Coroaba, N. Simionescu, C. M. Uritu, D. Bejan, L. E. Ursu, A.-I. Dascalu, F. Doroftei, M. Dobromir, C. Albu and C. O. Ania, Mn-Doped Carbon Dots as Contrast Agents for Magnetic Resonance and Fluorescence Imaging, *Int. J. Mol. Sci.*, 2025, **26**(13), 6293, DOI: **10.3390/ijms26136293**.

81 S. Sun, L. Zhao, D. Wu, H. Zhang, H. Lian, X. Zhao, A. Wu and L. Zeng, Manganese-Doped Carbon Dots with Red-shifted Orange Emission for Enhanced Fluorescence and Magnetic Resonance Imaging, *ACS Appl. Bio Mater.*, 2021, **4**(2), 1969–1975, DOI: **10.1021/acsabm.0c01597**.

82 H. Ding, J.-S. Wei, N. Zhong, Q.-Y. Gao and H.-M. Xiong, Highly Efficient Red-Emitting Carbon Dots with Gram-Scale Yield for Bioimaging, *Langmuir*, 2017, **33**(44), 12635–12642, DOI: **10.1021/acs.langmuir.7b02385**.

83 H. Ding, Y. Ji, J.-S. Wei, Q.-Y. Gao, Z.-Y. Zhou and H.-M. Xiong, Facile Synthesis of Red-Emitting Carbon Dots from Pulp-Free Lemon Juice for Bioimaging, *J. Mater. Chem. B*, 2017, **5**(26), 5272–5277, DOI: **10.1039/C7TB01130J**.

84 M. L. Essa, A. A. Elashkar, N. A. N. Hanafy, E. M. Saied and M. El-Kemary, Dual Targeting Nanoparticles Based on Hyaluronic and Folic Acids as a Promising Delivery System of the Encapsulated 4-Methylumbelliferone (4-MU) against Invasiveness of Lung Cancer in Vivo and in Vitro, *Int. J. Biol. Macromol.*, 2022, **206**, 467–480, DOI: **10.1016/j.ijbiomac.2022.02.095**.

85 M. A. Askar, N. M. Thabet, G. S. El-Sayyad, A. I. El-Batal, M. Abd Elkodous, O. E. El Shawi, H. Helal and M. K. Abdel-Rafei, Dual Hyaluronic Acid and Folic Acid Targeting PH-Sensitive Multifunctional 2DG@DCA@MgO-Nano-Core–Shell-Radiosensitizer for Breast Cancer Therapy, *Cancers*, 2021, **13**(21), 5571, DOI: **10.3390/cancers13215571**.